Computers in Biology and Medicine 104 (2019) 267–277

Contents lists available at ScienceDirect

Computers in Biology and Medicine

journal homepage: www.elsevier.com/locate/compbiomed

Ultrasound simulation model incorporating incident and reflected wave propagations along a common carotid artery

Li Deng[a], Yufeng Zhang[a,*], Zhengpeng Zhao[a], Kexin Zhang[b], Xiao Hu[a], Lian Gao[a], Hong Liang[a], Junhua Zhang[a]

[a] Department of Electronic Engineering, Information School, Yunnan University, Kunming, Yunnan, 650091, China
[b] The Second Affiliated Hospital of Kunming Medical University, Kunming, Yunnan, 650031, China

ARTICLE INFO

Keywords:
Local pulse wave propagation
Ultrasound simulation model
Reflected wave
Pulse wave velocity
Common carotid artery

ABSTRACT

An ultrasound simulation model incorporating incident and reflected wave propagations is proposed to provide a realistic data source for validation of transit time (TT)-based local pulse wave velocity (PWV) estimation algorithms. First, the incident wave (IW) and reflected wave (RW) at a certain position over a common carotid artery (CCA) are estimated. Then, the propagating pulse waves (PWs) along the CCA are modelled with the synthesizations of the estimated IWs and RWs, whose occurrences are delayed in opposite sequences according to a preset PWV. In ultrasound simulation, a geometric model of a CCA is built, and the dynamic scatterer models are constructed by moving the scatterer positions according to the synthesized PWs. The RF signals are generated using Field II. To characterize the PW propagations of different arterial stiffnesses consistent with clinical ones in the model, 30 healthy subjects from young, middle-aged, and elderly groups are recruited for extractions of IWs and RWs. To quantitatively verify the effectiveness of the simulation model, the normalized root-mean-squared errors (NRMSEs) are used to compare the estimated and preset PWs, time delays (TDs), and PWVs. Results show that for the three age groups, the estimated PWs, TDs, and PWVs conform to the preset ones with the mean NRMSEs of 0.92%, 18.47%, and 8.55%, respectively. Moreover, the model can characterize the effect of the wave reflection on the local PW propagation as its clinical manifestation. Therefore, the proposed model can be effective as a data source for the validation of TT-based local PWV estimation algorithms, particularly the effects of RWs on the estimation performance.

1. Introduction

Arterial stiffness is significantly associated with cardiovascular events in the general population [1], patients with coronary artery disease [2], hypertension [3–5], end stage renal disease [6], and impaired glucose tolerance [7]. Non-invasive quantifications of the arterial stiffness for the early diagnosis and effective prevention of cardiovascular events and related diseases are clinically important. The pulse wave velocity (PWV) is an important index for quantifying the artery stiffness because of its direct link to the elastic modulus of the artery [8]. Since the carotid artery is a frequent site of atheroma formation, the local carotid PWV could be considered a surrogate marker of carotid stiffness [8].

Owing to noninvasion and high frame rate, ultrasound-based techniques including loop [9–11] and transit time (TT) methods [12–14] have been developed for measuring the regional PWV. In loop methods, the PWVs are estimated from a linear segment in the early systolic phase of the loops formed with variations of flow-area and diameter-velocity [9]. The TT methods determine the local PWV from the time delay (TD) between the pulse waves (PWs) at two sites over a known distance along a segment of a common carotid artery (CCA). Owing to a simple principle, and the development of the ultrafast ultrasound imaging based on the plane wave technique, the TT method is preferable for the detection of the local PWV of a CCA with high temporal resolution and scan line density [15–19].

Fig. 1 shows the schematic diagram of the PW propagation from the left to right along a segment of a CCA scanned by an ultrasound probe. Owing to the superimposition of pressures, the PW is considered as the synthesization of the incident wave (IW) and reflected wave (RW) transmitting in opposite directions [20]. The IW is caused by the forward pressure wave deriving from heart constriction, while the RW is caused by the backward pressure waves reflected at any discontinuity along the arterial tree, such as carotid bifurcations, cerebral capillary, and area changes in arterial distensibility [21]. The RW of a CCA is

* Corresponding author. Yunnan University, Department of Electronic Engineering, Kunming, Yunnan Province, 650091, China.
E-mail address: yfengzhang@yahoo.com (Y. Zhang).

https://doi.org/10.1016/j.compbiomed.2018.11.009
Received 18 September 2018; Received in revised form 25 October 2018; Accepted 12 November 2018

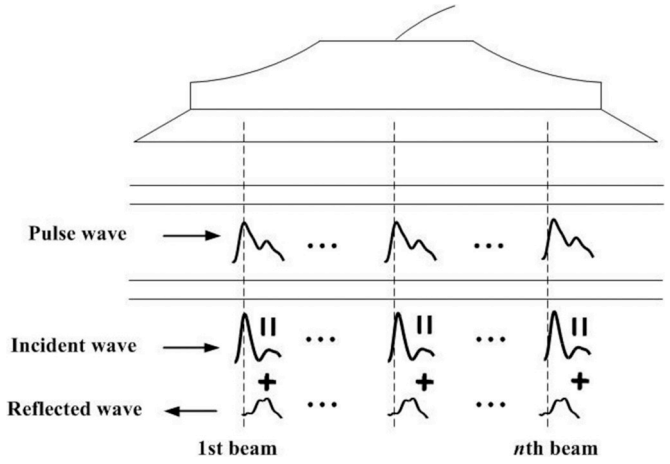

Fig. 1. Schematic diagram of the PW propagation from the left to right along a CCA scanned by an ultrasound probe. The PWs at different beam locations are the synthesizations of the IWs and RWs transmitting in opposite directions.

therefore a mixed component with the backward travelling waves occurring from systole to diastole periods of the IW [22]. In the TT method, the arterial segment is scanned by a linear-array transducer with n beams. The PWs at each beam is estimated from RF echo signal, and then the PWV is obtained based on the time fiduciary points (TFPs) in the PWs [17]. However, the RW is liable to change with the arterial elasticity, which leads to various PW deformations at different beam positions along the arterial segment. This obscures the TDs between PWs, and worsens the accuracy of the TT-based PWV estimation [23]. Additionally, the PW transmission distance along the CCA is short, and the accurate estimation of TDs is also difficult. Therefore, the investigation of ultrasonic TT method performance for the local PWV estimation under the influence of wave reflection is still a challenge and a research focus [13,17,23–26].

Ideally, studies on ultrasound scanning configurations and detection algorithms for the local PWV estimation of a CCA could be directly based on clinical data. However, it is limited since the true values (such as the RW, TD and PWV) are not known in clinics. Hence, flexible and realistic phantoms or simulation models are required to objectively and systematically investigate and evaluate the influence factors and algorithm performance. Several physical phantoms have been established to perform related evaluation studies. Meinders et al. [13] performed phantom experiments to verify a gradient method for the local PWV estimation. The phantom was set up in a water bath with a straight horizontal elastic tube. A hydraulic load and a half-filled buffer tank were connected with the two ends of the tube to reduce the reflections, and create a realistic pressure waveform, respectively. A pneumatic valve on the top of the buffer tank was used to generate a pulsatile increase in pressure. With changing the diameter of the tube, the different preset PWVs were yielded, and used to validate those estimated with an ultrasound system in experiments. In Hermeling et al.'s study [23], a phantom was built and scaled according to the realistic in vivo conditions to compare the performance of three TFP detection methods for the PWV estimation. The phantom setup consisted of a pulse generator, a water tank, and a water bath. A wave produced from the pulse generator propagated and ended in the elongated water bath. To measure the PWV, the propagating waves were simultaneously measured by an ultrasound probe facing upward at a small opening filled with silicone in the middle of the water bath. Results show that these physical phantoms can mimic the PW propagation under physiological conditions; however, they are limited to accurately characterize the local PW propagation of a CCA because of the inflexible configurations and unrealistic mimicking of the RW.

Computerized ultrasound models for PW propagation have also been applied in recent studies to investigate the effects of the ultrasonic scan parameters on the accuracy of the PWV estimation systematically. Huang et al. [27] performed PW propagation simulations to investigate the fundamental effects of several key parameters (i.e., the frame rate, motion estimation rate, number of scan lines, image width, PWV, and sonographic signal-to-noise ratio) on the performance of the local ultrasound-based PWV measurement. In the simulation, a PW obtained from a CCA of a healthy subject was assumed to propagate along the arterial wall from left to right. The convolution based image formation model was used to simulate the ultrasound RF signals with different preset parameters [28]. Then, the PWVs under the different parameter configurations were estimated by a PW imaging technique, and the performance of the PWV estimation was evaluated by measuring the relative errors and coefficients of variation and determination. In a previous study [29], an ultrasound simulation model was setup to investigate the effects of frame rate on the PWV estimation of a CCA. In the simulation, the Field II toolbox was used to calculate the pulsed ultrasound fields for RF signals by setting related parameters, such as frame rate, line density, excitations, etc. [30]. The B-scan ultrasonic sequence images of carotid artery with 16 scanning beams within an imaging width of 38 mm at the frame rates of 226 Hz, 376 Hz, 564 Hz and 1127 Hz were simulated. The performance was evaluated with a comparison between the estimated and preset values. In these computerized ultrasound models, the theoretical PWV and the values of the parameters related to the various influence factors can be preset. Experiments with these models are flexible and controllable through configuring model parameters, so evaluation studies can be conducted systematically. However, RW during the PW propagation along a CCA has not yet been considered in these computer ultrasound models.

To provide a realistic data source for the systematic study on the TT-based local PWV estimation of a CCA, particularly the effects of the RWs on the estimation performance, an ultrasound simulation model incorporating incident and reflected wave propagations is proposed in this study. The modelling process is as follow: first, the IW and RW are separated with the simultaneously measured PW and blood flow velocity of a CCA. Then, the propagating PWs at different beam positions along the CCA are modelled with the synthesizations of the IWs and RWs, whose occurrences are delayed in opposite sequences according to the preset PWV, respectively. To create a realistic ultrasound simulation, a geometric model of a CCA with a length of 39 mm is built, and the corresponding dynamic scatterer model is constructed by moving the scatterer according to the synthesized PWs at 13 beam positions. Then, the RF signals are generated in a dynamic scanning mode with a frame rate of 1333 Hz using the Field II platform. In order to characterize the PW propagations of different arterial stiffnesses, and simulate the PW propagations consistent with the clinical ones in the model, 30 healthy subjects from young, middle-aged, and elderly groups are recruited for the extraction of the IWs and RWs at a certain position over CCAs with an ultrasound diagnosis system. Accordingly, the PWVs of the three age groups are preset to 4.5, 6.0, and 7.0 m/s, respectively [10]. To quantitatively verify the effectiveness of the proposed simulation model, the PWs at 13 beam positions are estimated from the simulated RF signals with an echo tracking algorithm. The TDs are estimated based on the TFPs of maximum values of the second derivative (M2D) and the 20% threshold (TH20) in the estimated PWs [31]. The PWVs are estimated by a linear regression fit applied on the time-distance plot. Then, the normalized root-mean-squared errors (NRMSEs) between the estimated and preset PWs, time delays (TDs), and PWVs are calculated, respectively. The performance of the presented model is assessed with the mean values and standard deviations (SDs) for the NRMSEs of these three indexes.

2. Modelling methods

In this study, an ultrasound simulation model for PW propagation along a CCA with a synthesization of IW and RW transmitting in opposite directions is proposed. A block diagram for illustrating the

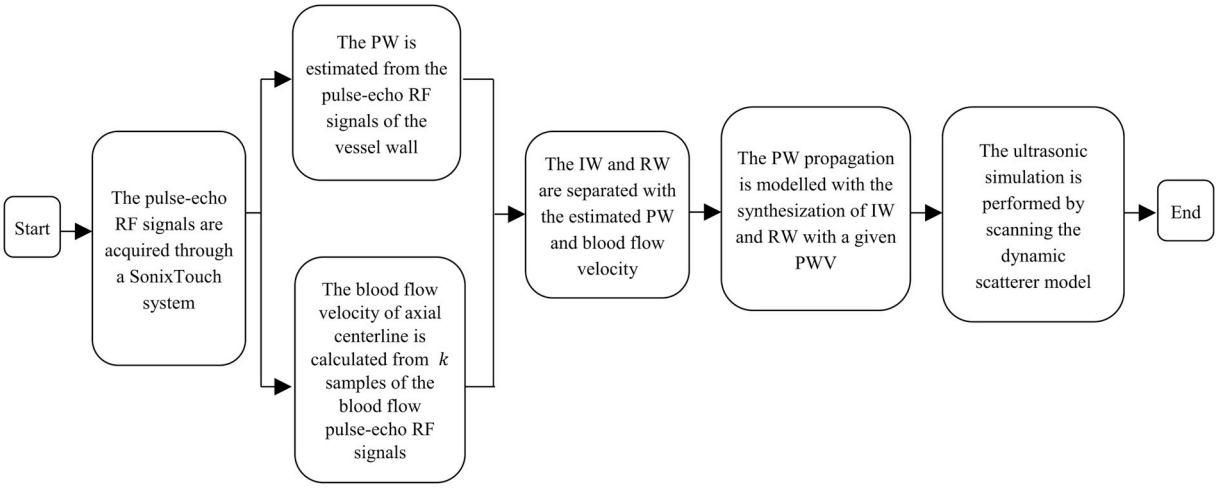

Fig. 2. Block diagram illustrating the establishment procedure of the ultrasound simulation model for the PW propagation along a CCA based on the Field II.

establishment procedure of the model is shown in Fig. 2. In order to obtain the IWs and RWs with propagating characteristics conforming to clinical ones in modelling, the pulse-echo RF signals at a certain position of the human CCA are first measured using a SonixTOUCH system (Ultrasonix Medical Corporation, Richmond, B.C., Canada). Then, the PW and blood flow velocity of the axial centerline are estimated from the pulse-echo RF signals of the vessel wall and blood flow, respectively. Next, the IW and RW are obtained using the estimated PW and blood flow velocity. To model a realistic local PW propagation, the PW at each beam position is synthesized by the IW and RW, whose occurrences are delayed in the opposite sequences with a given PWV. Finally, the ultrasound simulation of the PW propagation is performed by the Field II platform used for scanning the dynamic scatterer models constructed based on the synthesized PWs.

2.1. Estimations of PW and blood flow velocity from human subject

To estimate simultaneous PW and blood flow velocity, the SonixTouch RP ultrasonic system is used to acquire the pulse-echo RF signals at a certain position of human CCAs. The PW is estimated from the pulse-echo RF signals of the vessel wall using a 1-D normalized cross-correlation (NCC) algorithm based on echo tracking. A reference RF signal is defined in one frame, and subsequently contrasted with the comparison RF signals from another frame within a pre-specified search range. The reference and comparison RF signals in the different frames (time) are $f(n)$ and $g(n)$, respectively. The similarity or matching between the reference and comparison signals is quantified by the NCC coefficient [32].

$$R_{NCC}(\tau) = \frac{\sum_{n=u}^{u+w-1} f(n)g(n+\tau)}{\sqrt{\sum_{n=u}^{u+w-1} f^2(n) \sum_{n=u}^{u+w-1} g^2(n+\tau)}} \quad \tau_1 \le \tau \le \tau_2 \tag{1}$$

The parameter u is the origin of the reference window, and w is the window size. The parameter τ is the shift between the comparison and reference windows, and $[\tau_1, \tau_2]$ is the search range determined by the maximum range of the radial distensions of the vessel wall. The signal $f(n)$, which represents the vessel wall in the frame farthest from the probe, is selected manually within the interval of $[u,\ u+w-1]$. The wall motion for the nth frame (time) is estimated from the spatial shift between the $f(n)$ and the best-matched $g(n)$ at the nth frame in terms of the maximum value of $R_{NCC}(\tau)$ in the research region of $[\tau_1, \tau_2]$. Based on the wall motion at each frame, the PW during a cardiac cycle is obtained. To reduce the quantization noise, the estimated PW is filtered with a Savitzky-Golay digital smoother [33]. The blood flow velocity of the axial centerline is estimated from the K samples of the blood flow pulse-echo RF signals using an autocorrelation estimator. In this process, the quadrature demodulation of the RF signals is performed to determine their envelopes with the Hilbert transform.

$$R = r(k) + j * i(k) \quad 1 \le k \le K \tag{2}$$

The parameter j is equal to $\sqrt{-1}$, and k is the sampling time. $r(k)$ and $i(k)$ denote the in-phase and quadrature components of the envelopes at time k, respectively. Then, the phase shift φ of the demodulated pulse-echo RF signal caused by the flowing blood cells is estimated by the autocorrelation algorithm [34].

$$\varphi = arctan\left(\frac{\sum_{k=2}^{K} i(k)r(k-1) - r(k)i(k-1)}{\sum_{k=2}^{K} r(k)r(k-1) + i(k)i(k-1)}\right) \tag{3}$$

The corresponding blood flow velocity is calculated by the equation below.

$$v = -\frac{cf_{prf}}{4\pi f_0}\varphi \tag{4}$$

The parameter c is the ultrasound velocity. The terms f_{prf} and f_0 are the pulse repetition frequency and the center frequency, respectively. Finally, the blood flow velocity waveform during a cardiac cycle is obtained with the estimated velocity at the time corresponding to the frame (time) for the detection of the wall motion.

2.2. Extractions of IW and RW

With measured pressure, or wall diameter, or wall distension, and blood flow velocity waves, several methods have been introduced to separate forward and backward waves [22,35–37]. In the present study, a simple velocity- and distension-based upstroke fitting method [37] is used to extract the IW and RW of a CCA. The procedure for this method consists of three steps.

Step 1: The blood flow velocity and PW are simultaneously measured as a function of time.
Step 2: The pressure wave is calculated using an estimated varying cross-section of the blood vessel. First, the cross-section of the blood vessel is obtained by solving the equation of the 1-D transformed conservation of mass [38].

$$\frac{\partial A}{\partial t} - \frac{1}{c}\frac{\partial (Au)}{\partial t} = 0 \tag{5}$$

The parameters t and c are time and average aortic PWV, respectively. The terms A and u are the cross section of the blood vessel and the normalized blood flow velocity at the central position, respectively. Then, the elastic model [38] is used to convert the changes in the cross

section of the blood vessel into the pressure.

$$P(t) - P_0 = \frac{1}{Cs}[A(t) - A_0] \tag{6}$$

The constant Cs is the compliance of the vessel wall. The parameters A_0 and P_0 are the initial values of the cross section and pressure, respectively.

Step 3: The RW is extracted by subtracting the estimated normalized IW from the normalized PW. The distension waveform at each relaxation time caused by the estimated pressure wave is estimated using the Kelvin-Voigt model [37]:

$$\varepsilon(t) = \frac{1}{\vartheta} exp\left(-\frac{1}{\tau}t\right) \int_0^k (P(t) - P_0) exp\left(\frac{1}{\tau}t\right) dt \tag{7}$$

The parameter $\varepsilon(t)$ is the distension component, and ϑ and τ are the viscosity constant and relaxation time, respectively. The term $1/\tau$ is used to optimize the fitting of the increasing portion of the calculated distension waveforms. Because the upstroke of the PW is composed of the significant IW and little RW, whereas the upstroke of the blood flow velocity of the axial centerline is caused by the IW [39], the IW is determined with the most similarity in the upstrokes of the calculated distension waves to the PW. Then, the RW is the difference between the normalized PW and IW.

2.3. Modelling the propagation of the PW

The PW at each beam position is the synthesization of the IW and RW propagating in opposite directions along a segment of the CCA. As shown in Fig. 1, assuming that the measured PW and blood flow velocity waveform are generated at the first beam position along a segment of the CCA with a length of d mm, which is scanned by a linear-array transducer with N beams, then the IW and RW at this position can be estimated by the algorithm introduced in Section 2.2. Based on a preset PWV, the TD for the IW propagating from left to right, (or the RW propagating in the opposite direction) between the adjacent beam positions is given by the equation below.

$$\Delta t = \frac{d}{(N-1) * PWV_{pst}} \tag{8}$$

The term PWV_{pst} is the preset value of the PWV. Then, the IW and RW at the i th beam position are expressed as shown below.

$$\varepsilon_i = \varepsilon_1(t + \Delta t * (i-1)), \quad (i = 1,2, \cdots\cdots, N) \tag{9}$$

$$\sigma_i = \sigma_1(t - \Delta t * (i-1)), \quad (i = 1,2, \cdots\cdots, N) \tag{10}$$

The parameters $\varepsilon_1(t)$ and $\sigma_1(t)$ are the normalized IW and RW at the first beam position, respectively. Finally, the normalized PW at the i th beam position is calculated by the following equation.

$$\gamma_i = \varepsilon_i + \sigma_i \tag{11}$$

Thus, the propagation of the PW from left to right along a segment of the CCA is modelled.

In practice, the RW has the varying amplitude and PWV depending on the different degree of the arterial stiffness. Moreover, different amplitudes and PWVs of RW result in various deformations in the PWs at different beam positions. In order to describe these characteristics in modelling, healthy subjects from young, middle-aged, and elderly groups are recruited for the extraction of the IWs and RWs from CCAs because the artery stiffness increases with aging. The preset PWVs for these three groups are given according to a relationship between the age and PWV [10]. Based on these clinical data, the ultrasound simulation model incorporating IW and RW propagations with the characteristics conforming to clinical versions is established.

2.4. Ultrasound simulation of PW propagation

To create a realistic simulation, the ultrasound simulation software platform Field II running within the MATLAB (The Mathworks Inc., Natick, Massachusetts, USA) environment is used to simulate the PW propagation along a CCA scanned by the ultrasound. Then, the ultrasound RF signals are generated by temporal and spatial convolutions of the excitation, acoustic fields, and point scatterers [40].

$$v_r(t) = v_{pe}(t) *_t f_m(\vec{r_1}) *_r h_{pe}(\vec{r_1}, t) \tag{12}$$

The parameter $*_t$ denotes the temporal convolution, and $*_r$ represents the spatial convolution. The parameter $\vec{r_1}$ expresses the position of the point scatterer, and $v_{pe}(t)$ is the transducer excitation and the electro-mechanical impulse response during the emission and reception of the pulse. The parameter f_m is the spatial position function of the point scatterers that accounts for the inhomogeneities in the tissue, and h_{pe} is the pulse-echo spatial impulse response.

The ultrasound simulation for the PW propagation involves building the geometric model, creating the dynamic tissue scatterer model, and generating the RF signals. First, a pair of concentric cylinders with a length of L is constructed to model the CCA with internal and external diameters of D_1 and D_2, and placed in the center of a cuboid phantom with a size of $L \times W \times H$. Then, the scatterers with the intensity, which follows a normal distribution, but has different strengths for the vessel wall and surrounding tissue, are randomly and uniformly placed in the phantom. By applying the amplitudes of PWs at each scan frame on the corresponding scatterers based on the PW propagation model according to Eq. (11), the dynamic tissue scatterer model is established by updating the scatterer positions dynamically. Finally, the ultrasound RF echo signals for the PW propagation are simulated based on Field II. For the realistic purpose, white Gaussian noise is added to the simulated RF signals with a prespecified signal-to-noise ratio (SNR) of 10 dB.

3. Results

3.1. Estimations of the PW and blood flow velocity from the human subject

In order to simulate the PW propagations of different arterial stiffnesses consistent with the clinical ones, the PWs and blood flow velocities are first estimated with the pulse-echo RF signals measured from human CCAs. 30 sets of signals are measured using the SonixTOUCH system with a L14-5w/60 linear-array transducer from CCAs of 30 healthy human subjects: 10 young (age 24 ± 3 years), 10 middle-aged (age 45 ± 5 years), and 10 elderly (age 63 ± 4 years) volunteers. The measurements are performed after 10 min of rest in a supine position. To observe the motions of the wall vessel and blood flow in real-time, the system runs a pulse wave Doppler (PWD) duplex sequence that is displayed by adjusting the sampling gate in real-time on the B-mode image. Fig. 3 shows a Doppler spectrum for the PWD duplex sequence sampled with a gate marked by green lines covering the CCA on the B-mode image. Table 1 lists the imaging parameters of the PWD and B-mode used in the SonixTOUCH system. The size of the PWD gate ranges from 11 to 14 mm for the different CCA diameters to meet the requirement of simultaneous measurements of the PW and blood flow velocity of the vessel. The RF echo signals are digitized at a sampling frequency of 40 MHz. Then, the PWs are estimated from the pulsed-echo RF signals of the vessel walls by Eq. (1), and the blood flow velocities are calculated from 64 samples of the blood flow pulse-echo RF signals by Eqs. (2)–(4).

Fig. 4 (a), (b), and (c) show the normalized PWs (solid line) and blood flow velocity waveforms (dashed line) measured from the CCAs of three healthy subjects 24, 45, and 63 years old, respectively. In these figures, there are significant differences in the PWs and blood flow waveforms from the different ages. For all three PWs, there are three peaks caused by the IW, RW, and dicrotic notch. However, although the

Fig. 3. Clinical Doppler spectrum image combined with a B-mode image from the CCA of a 63-year-old subject.

Table 1
Imaging parameters of the PWD and B-mode used in the SonixTOUCH system.

Type	Parameter name	Parameter value
PWD	Gain	70%
	PRF	5 KHz
	The center frequency	5 MHz
	The cutoff frequency of wall filter	175 Hz
	Sampling angle	0^0
	Steer angle	45^0
	Gate	11–14 mm
B-mode image	The center frequency	10 MHz
	Depth	45 mm
	Width	60 mm
	Frame rate	166 Hz
	Gain	62%
	Dynamic range	70 dB
	Ultrasound velocity	1540 m/s

first peak observed in the PW of the 24-year-old is distinct, the others are vague and broad for the elder subjects. In addition, the second peak is smaller for the young subject than those of the elder subjects, especially for the 63-year-old subject. This is because the second peak in the PW is caused by the RW, whose amplitude and PWV increase with the increased arterial stiffness of the elder subjects. The blood flow velocity waveforms consist of two phases: systole and diastole. In general, the arrival time of the blood flow is earlier than that of the PW because of the viscous property of the blood vessel. The first peaks caused by the ejection of the blood flow are located between the upstroke and downstroke of the systole phase and are observed for all ages. The second peaks caused by the RWs must, theoretically, appear in the systolic downstroke of the flow waveforms. However, this peak is not apparent for the 24-year-old subject owing to the minimal effect of the RW.

3.2. Extractions of IW and RW

With the measured PWs and blood flow velocity waveforms, the IWs are extracted from the PWs by the velocity- and distension-based upstroke fitting method, and then the RWs are obtained by the differences between the PWs and calculated IWs. Fig. 5 (a), (b), and (c) show the IWs (dash-dotted lines) and RWs (dashed lines) separated from the PWs (solid lines) for the same 24-, 45- and 63-year-old subjects as those in Fig. 4. The shapes of the IWs during the systolic upstroke are similar to those of the PWs because the upstroke of the PW is mainly caused by the blood flow from heart contraction [41]. However, the amplitudes of the RWs are small at the beginning of the upstroke, and last to the end of the diastole. The maximum amplitudes of the RWs for the elder subjects are greater than those of the young subjects, which is the main reason influencing the deformations in the peak of the pulse wave. These characteristics are in agreement with previous studies, where the amplitude of the RW increases with the age-related stiffening of the arterial elasticity [22,36,37].

3.3. Modelling the propagation of the PW

Based on the relationship between the PWV and age reported in previous studies [10,42], the PWVs for healthy human subjects range from 4.3 to 4.7 m/s for the young group, 5.5–6.2 m/s for the middle-aged group, and 6.8–7.3 m/s for the elderly group. Thus, the PWVs of 4.5 m/s, 6.0 m/s, and 7.0 m/s are preset to the ten young, middle-aged, and elderly volunteers for modelling the PW propagation, respectively. Ideally, the high frame rate and high line density in ultrasound scanning meet the requirement of a high temporal and spatial resolution for wall motion tracking, and thus, an accurate TT-based local PWV estimation is produced [18,19]. As a reasonable tradeoff, a L14-5w/60 linear-array transducer used in this study can create a frame rate of 1333 Hz with 13 scan lines. For a realistic simulation, a configuration of the PWs from 13 beam positions along a 39 mm CCA using ultrasound scanning at the frame rate of 1333 Hz is considered in the modelling. Thus, the TDs between the adjacent beams calculated by Eq. (8) are 0.72 ms, 0.54 ms, and 0.46 ms for the PWVs of 4.5 m/s, 6.0 m/s, and 7.0 m/s, respectively. Based on these TDs, the corresponding IWs and RWs (which are travelling in opposite directions) at different beam positions are estimated by Eqs. (9) and (10), and then summed to yield the PW at each beam position. With the maximum radial distension of 0.4 mm [13] for the CCA during a cardiac cycle, the PW propagations for these three age groups are modelled. Fig. 6 (a), (b), and (c) show the PW propagations at 13 different beam positions during a cardiac cycle with preset PWVs of 4.5 m/s, 6.0 m/s, and 7.0 m/s synthesized with the IWs and RWs of the 24-year-old, 45-year-old, and 63-year-old subjects shown in Fig. 5. The insets show the magnified first peaks (red circles) of PWs indicated by the dotted rectangles in (a), (b) and (c). The linear

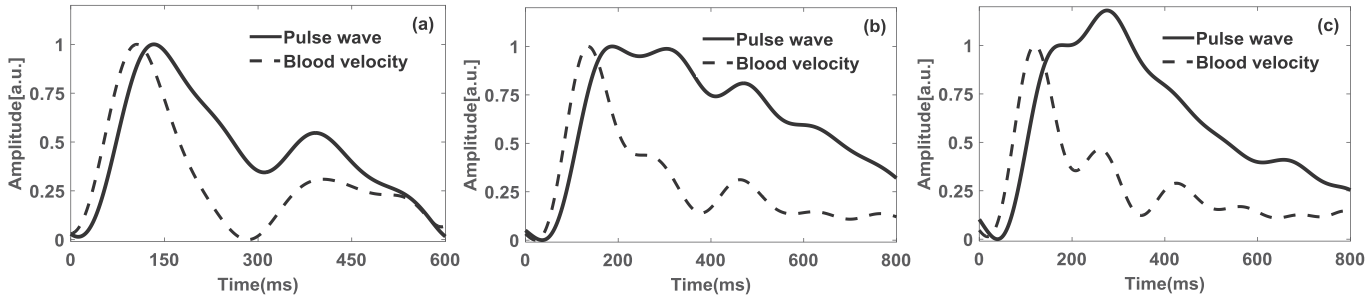

Fig. 4. Normalized PWs (solid line) and blood flow velocity waveforms (dashed line) measured from the CCAs of the 24-year-old (a), 45-year-old (b), and 63-year-old (c) subjects.

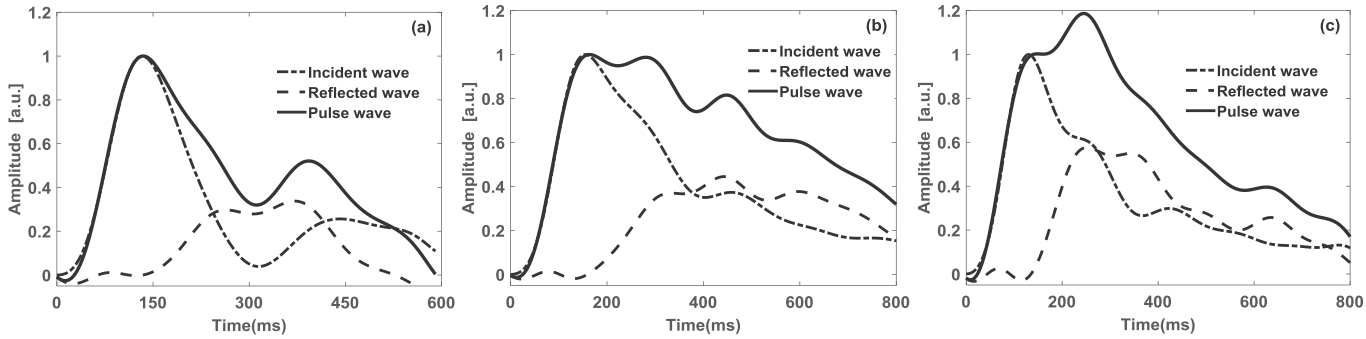

Fig. 5. IWs (dash-dotted line), RWs (dashed line), and PWs (solid line) for the 24-year-old (a), 45-year-old (b), and 63-year-old (c) subjects, respectively. They are estimated from the PWs and blood flow velocity waveforms shown in Fig. 4.

fitting lines with the red circles show the TDs between the PWs at different beam positions. It can be observed that the slopes of the linear fitting lines gradually get bigger from (a) to (c). This demonstrates that the PWVs increase gradually from (a) to (c), which is consistent with the PWVs preset to the 24-year-old (a), 45-year-old (b), and 63-year-old (c) subjects in Fig. 5. Moreover, the variations in the locations of red circles deviating from the fitting lines become gradually larger from (a) to (c). This is because the deformation in the upstroke of the PW for the elder subject is larger than that for the young subject.

3.4. Ultrasound simulation based on the Field II program

In the ultrasound simulation, a geometric model of a CCA with a length of 39 mm is created, as shown in Fig. 7. In this model, the concentric cylinder represents a blood vessel with the length of 39 mm and the thickness of 1.25 mm, and the remaining portion of the cuboid phantom with the dimensions of 39 × 12 × 25 mm is for the surrounding tissue. The tissue scatterer model is generated by a total of 6×10^6 point scatterers with a density of 5 scatterers/λ^3 (λ is the wavelength) randomly and uniformly placed in the geometric model, in which the positions and amplitudes are uniform and Gaussian in distributions, respectively. The intensity of the scatterers of the vessel walls is set to five times the intensity of the surrounding tissue, and the amplitude of the blood flow is set to zero for its minimal effect on the model. By moving the scatterer positions according to the amplitude of PW at each beam and frame from the PW propagation models, the dynamic sequence scatterer models for the different age groups are constructed. Finally, based on the series of B-mode imaging and ultrasonic probe parameter settings listed in Table 2, the RF echo signals corresponding to the dynamic sequence scatterer models are generated

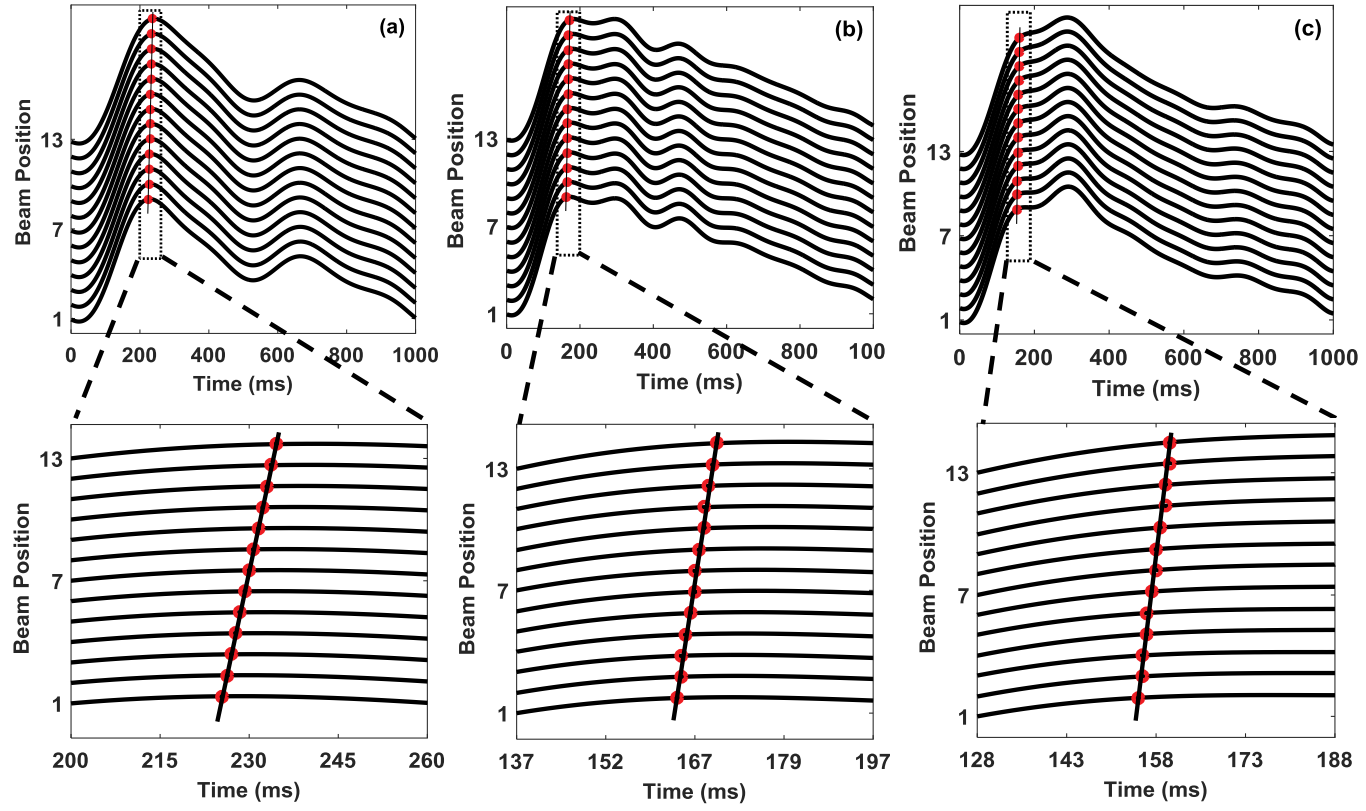

Fig. 6. Synthesized PWs at 13 beam positions within a cardiac cycle propagating with different PWVs based on the IWs and RWs shown in Fig. 5. The preset PWVs of 4.5 m/s (a), 6.0 m/s (b), and 7.0 m/s (c) are given for the 24-year-old (a), 45-year-old (b), and 63-year-old (c) subjects, respectively. The insets represent the magnifications of the first peaks (red circles) of PWs indicated by the dotted rectangles in (a)~(c). The linear fitting lines indicate the delays due to the PW propagations.

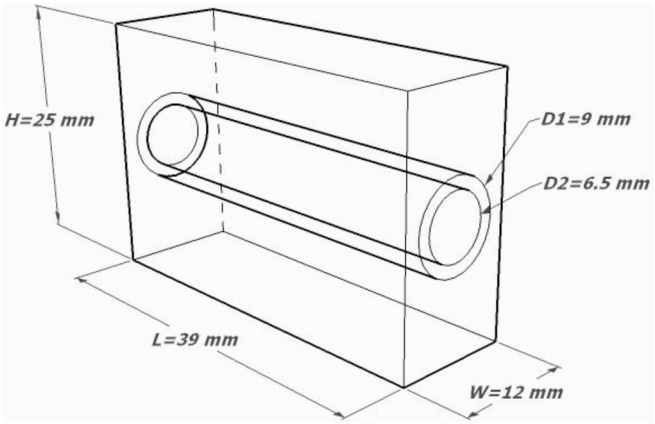

Fig. 7. Geometric model of a segment of the CCA.

Table 2
Parameters of the B-mode imaging and ultrasonic probe used in the ultrasound simulation based on the Field II program.

Type	Parameter name	Parameter value
B-mode imaging	The center frequency	10 MHz
	The sampling frequency	100 MHz
	Depth	25 mm
	Width	39 mm
	Frame rate	1333 Hz
	Line density	13
	Wavelength	1.54×10^{-4} m
	Ultrasound velocity	1540 m/s
Ultrasonic probe	The width of element	0.77×10^{-4} m
	The height of element	0.005 m
	Distance between elements	1.54×10^{-5} m
	Number of physical elements	256
	Number of active elements	64
	Fixed focal point	[0 0 0.03] m
	Focal zones for reception	[0.03:0.02:2] m

by Eq. (12). Fig. 8 (a)–(f) show the simulated ultrasound RF signals with SNR = 10 dB for the 24-year-old ((a), (d)), 45-year-old ((b), (e)), and 63-year-old ((c), (f)) subjects, whose PW propagation models are shown in Fig. 6. The amplitudes of the RF signals of the arterial walls are greater than those of the surrounding tissue. The signals in Fig. 8 (a)–(c) are produced in the time of the first frame (green signals) and the frame corresponding to the maximum radial distension (red signals) for the first beam position. The spaces between the red RF signals of the arterial walls are larger than those of the green ones, which indicate that the vessel is expanding with time. Fig. 8 (d)–(f) are generated from the first (green signals) and the 13th (red signals) beam positions at the time of the 125th frame which corresponds to the scanning time in the early systole. The red RF signals of the arterial wall shift slightly to the right of the green signals, which means the radial distension at the 13th (red signals) beam position lags behind that at the first beam position when the scanning time is the 125th frame. This indicates that the propagation of the PW is from left to right along the segment of the artery. Thus, the motions of the RF signals of the vessel wall agree with those of the dynamic pulsation in the PW propagation model shown in Fig. 6.

3.5. Quantitative evaluation of the ultrasound simulation model

To evaluate the performance of the established ultrasound simulation model for a PW incorporating IW and RW propagating along a CCA, three indexes of PW, TD and PWV are estimated based on the simulated RF signals. Quantitative evaluations are performed by the mean values and SDs for NRMSEs of the three indexes between the estimated results and preset values. The PWs at the 13 beam positions for each simulation are tracked from the simulated RF signals by Eq. (1) and are filtered by the Savitzky-Golay digital smoother [33]. Then, the TDs of the PWs between two adjacent beam positions are estimated with the TH20 and M2D methods, respectively. Finally, the PWVs are calculated by a linear regression fit applied on the time-distance plot. The PWs in Fig. 9 (a), (b), and (c) are estimated from the simulated RF signals in Fig. 8, which corresponding to the dynamic sequence scatterer models with the preset PWVs of 4.5 m/s (a), 6.0 m/s (b), and 7.0 m/s (c) for the 24-year-old (a), 45-year-old (b), and 63-year-old (c) subjects, respectively. Fig. 10 (a), (b), and (c) show the PWs filtered from those in Fig. 9 (a), (b), and (c), respectively. Table 3 lists the mean values and SDs for the NRMSEs between the estimated and theoretical PWs for different beam positions and age groups over 10 simulations. The measurement of PWs at the 13 beam positions can be estimated accurately with lower NRMSEs of 1.07 ± 0.01 %, 0.86 ± 0.01 %, and 0.83 ± 0.01 %, for the young, middle-aged, and elderly groups, respectively. These errors are caused by the randomness of the ultrasonic RF echo signals from the vessel wall and the performance of the echo tracking algorithm. The means and SDs of the NRMSEs between the preset and estimated TDs for the young, middle-aged, and elderly groups are listed in Table 4. They are 10.37 ± 0.55 %, 9.12 ± 0.58 %, and 20.99 ± 0.59 % for the TH20 method, and 12.89 ± 0.51 %, 28.90 ± 0.70 %, and 28.52 ± 0.95 % for the M2D method, respectively. The errors of elderly group are both larger than those of the younger groups. This is because that the amplitudes and PWVs of RWs for elderly group are greater than those of the younger groups. Larger and faster RWs cause more different deformations in the PWs, which affect the locations of the TFPs in different PWs. Moreover, the TH20-based errors are smaller than those based on M2D. This indicates that under the influence of the RWs, the performance of TD detection based on different TFPs is different. Therefore, the proposed model can characterize the effect of RWs on PWs propagation along a CCA. This model can be used to evaluate the performance of TD detections with different TFPs.

The PWVs are estimated by a linear regression fit applied on the time-distance plot. As shown in Fig. 11, the inverse of the slopes of the fitted lines based on the TDs for the filtered PWs shown in Fig. 10 are the PWV estimates: 4.48 m/s (a), 5.76 m/s (b), and 6.74 m/s (c) and the corresponding coefficient correlations of 0.996, 0.981, and 0.976 for TH20; 4.56 m/s (d), 5.02 m/s (e), and 5.89 m/s (f) and the corresponding coefficient correlations of 0.956, 0.952, and 0.947 for M2D. The estimated PWVs are generally in accordance with the preset ones. Based on 30 human subjects, the means and SDs of the NRMSEs between the estimated and preset PWVs for the three age groups are computed and shown in Fig. 12. For the young, middle-aged, and elderly groups, they are 1.36 ± 2.52 %, 3.70 ± 2.39 %, and 13.88 ± 3.74 % for the TH20 method and 4.90 ± 3.01 %, 11.44 ± 4.21 %, and 16.01 ± 3.63 % for the M2D method, respectively. In general, the PWV errors estimated with the two methods for the three age groups are different. Their variations are in accordance with those in TDs. However, with linear fitting, the PWV errors are all reduced in different extent compared with those of TDs. In addition, the estimated PWVs for the young group exhibit a higher precision with errors less than 8%. With an increase of the age (increases preset PWV and RW amplitude), the errors of the estimated PWVs by the two methods increase. The increments for the middle-aged and elderly groups are 2.34 % and 12.52 % for the TH20 method and 6.54 % and 11.11 % for the M2D method, respectively. This is because the increased RW amplitude and PWV caused by aging obscure the time-shift between the waveforms and then affect the accuracy of the TT-based PWV estimation. By contrast, as a simple and ideal model [27,29], in which only the IW is involved as the PW propagating along the artery, the error of the estimated PWV is approximate 2%–7%. Therefore, the model can characterize the effect of the wave reflection on the local PW propagation as its clinical manifestation.

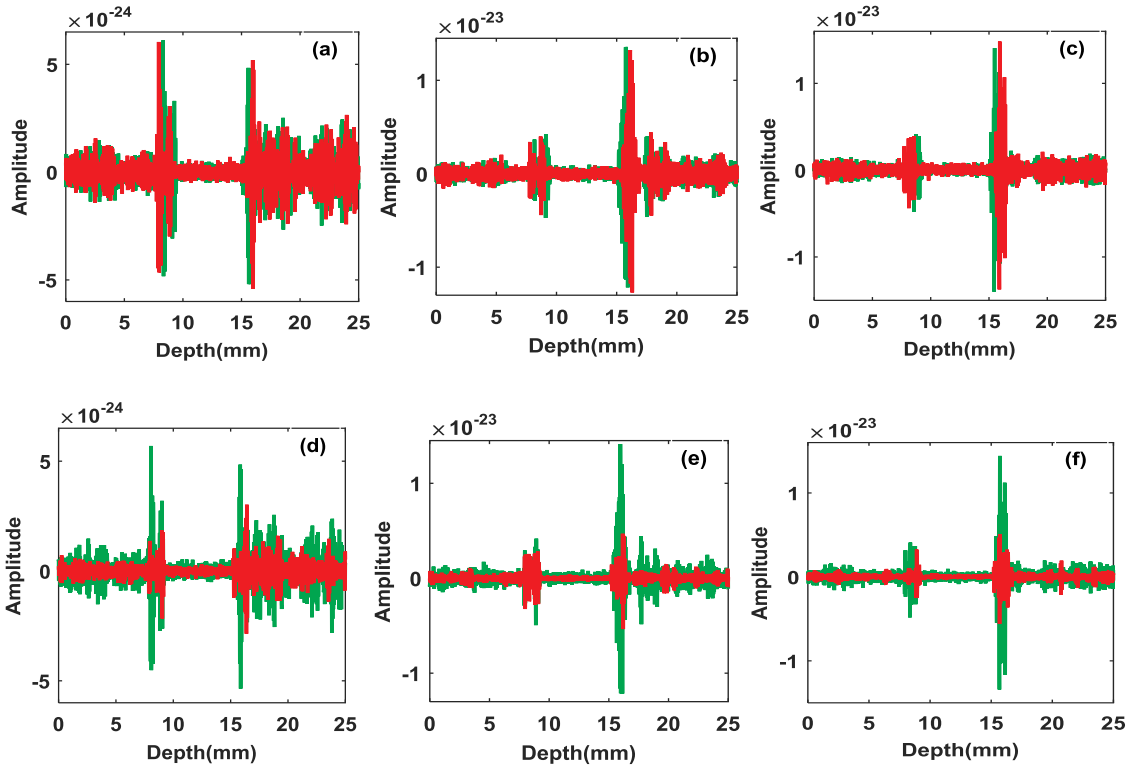

Fig. 8. Simulated ultrasound RF signals in Figs. (a)–(c) generated in the time of the first frame (green signals) and the frame with the maximum radial PW (red signals) at the first beam position and in Figs. (d)–(f) generated at the first beam position (green signals) and the 13th beam position (red signals) in the 125th frame, which correspond to the 24-year-old ((a), (d)), 45-year-old ((b), (e)), and 63-year-old ((c), (f)) subjects, respectively. Note that the units of amplitude are dimensionless.

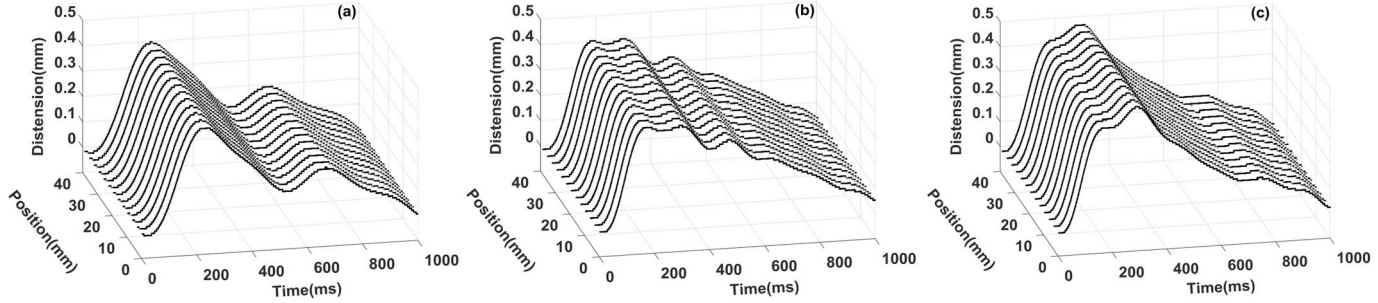

Fig. 9. PWs estimated from the simulated RF signals with the preset PWVs of 4.5 m/s (a), 6.0 m/s (b), and 7.0 m/s (c), which correspond to the 24-year-old (a), 45-year-old (b), and 63-year-old (c) subjects, respectively, at 13 different beam positions within a cardiac cycle.

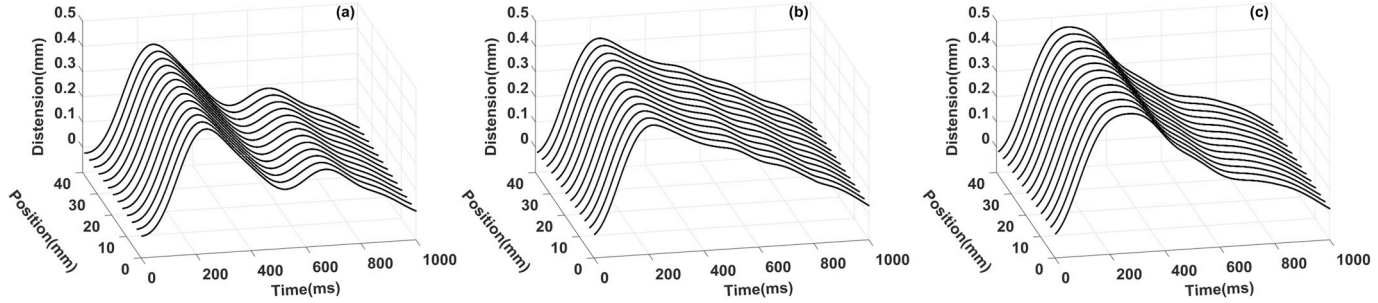

Fig. 10. Filtered PWs with the Savitzky-Golay digital smoother from the results in Fig. 9. The preset PWVs are 4.5 m/s (a), 6.0 m/s (b), and 7.0 m/s (c) for the 24-year-old (a), 45-year-old (b), and 63-year-old (c) subjects, respectively.

4. Discussions

As a non-invasive technique, the ultrasonic TT method for regional PWV measurement of CCAs has been intensively studied [17]. A realistic simulation model is required as a data source for the evaluation of processing algorithms and effect factors systematically. Owing to the short transmission distance and special structures such as the carotid bifurcation, high resistance of cerebral capillary, etc., the RW of a CCA

Table 3
Mean ± SD for the NRMSEs between the estimated and theoretical PWs for the different beam positions and age groups over the 10 simulations.

Beam No.	Mean ± SD of NRMSEs (%)		
	Young group	Middle-aged group	Elderly group
1	1.07 ± 0.01	0.87 ± 0.03	0.83 ± 0.01
2	1.08 ± 0.01	0.84 ± 0.02	0.86 ± 0.01
3	1.08 ± 0.01	0.83 ± 0.01	0.85 ± 0.01
4	1.08 ± 0.01	0.84 ± 0.01	0.82 ± 0.02
5	1.08 ± 0.01	0.86 ± 0.01	0.83 ± 0.01
6	1.07 ± 0.02	0.88 ± 0.01	0.83 ± 0.01
7	1.06 ± 0.01	0.88 ± 0.01	0.82 ± 0.01
8	1.05 ± 0.01	0.86 ± 0.01	0.82 ± 0.01
9	1.04 ± 0.01	0.85 ± 0.01	0.82 ± 0.01
10	1.04 ± 0.01	0.84 ± 0.01	0.82 ± 0.01
11	1.05 ± 0.01	0.85 ± 0.02	0.83 ± 0.03
12	1.09 ± 0.03	0.89 ± 0.02	0.82 ± 0.01
13	1.08 ± 0.01	0.84 ± 0.01	0.82 ± 0.01

Table 4
Mean ± SD for the NRMSEs between the TDs estimated using the TH20 and M2D methods over the 10 simulations for the three age groups.

Age groups	Mean ± SD for NRMSEs (%)	
	TH20	M2D
Young group	10.37 ± 0.55	12.89 ± 0.51
Middle-aged group	9.12 ± 0.58	28.90 ± 0.70
Elderly group	20.99 ± 0.59	28.52 ± 0.95

is significant and varying in amplitude and transmitting velocity. It influences the accuracy of the TT-based local PWV estimation because the varying amplitude and PWV with the arterial stiffness result in various variations in the PWs at different beam positions. However, RW has not yet been taken account into the computer ultrasound simulation

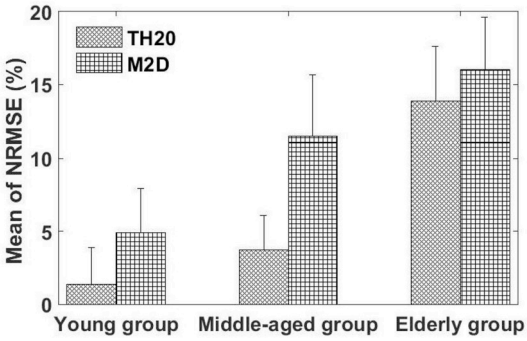

Fig. 12. Mean and SD bars of the NRMSEs between the PWVs estimated using the TH20 and M2D methods based on the simulations with the 30 human subjects. The preset PWVs are 4.5 m/s, 6.0 m/s, and 7.0 m/s for the young, middle-aged, and elderly groups, respectively.

models for PW propagation proposed in our previous study [29] and the convolution-based method [27]. In the present study, an ultrasound simulation model incorporating incident and reflected wave propagations is proposed to provide a realistic data source for validation of TT-based local PWV estimation algorithms. For the first time, a synthesization of the IW and RW transmitting along a CCA is proposed to model the PW propagation. The experimental results demonstrate that the proposed model can characterize the effect of wave reflection on the local PW propagation along CCAs. In present modelling, a velocity- and distension-based upstroke fitting method proposed by Masashi Saito et al. is used for IW and RW extractions based on the simultaneous PW and blood flow velocity. According to an elastic model, the pressure wave is estimated from the blood flow velocity. A Kelvin-Voigt model is used to calculate the displacement waves at different relaxation times caused by the pressure wave. Then, the IW is determined with the most similarity in the fitting of the upstrokes of the calculated displacement waves to the PW. The RW is the difference between the PW and

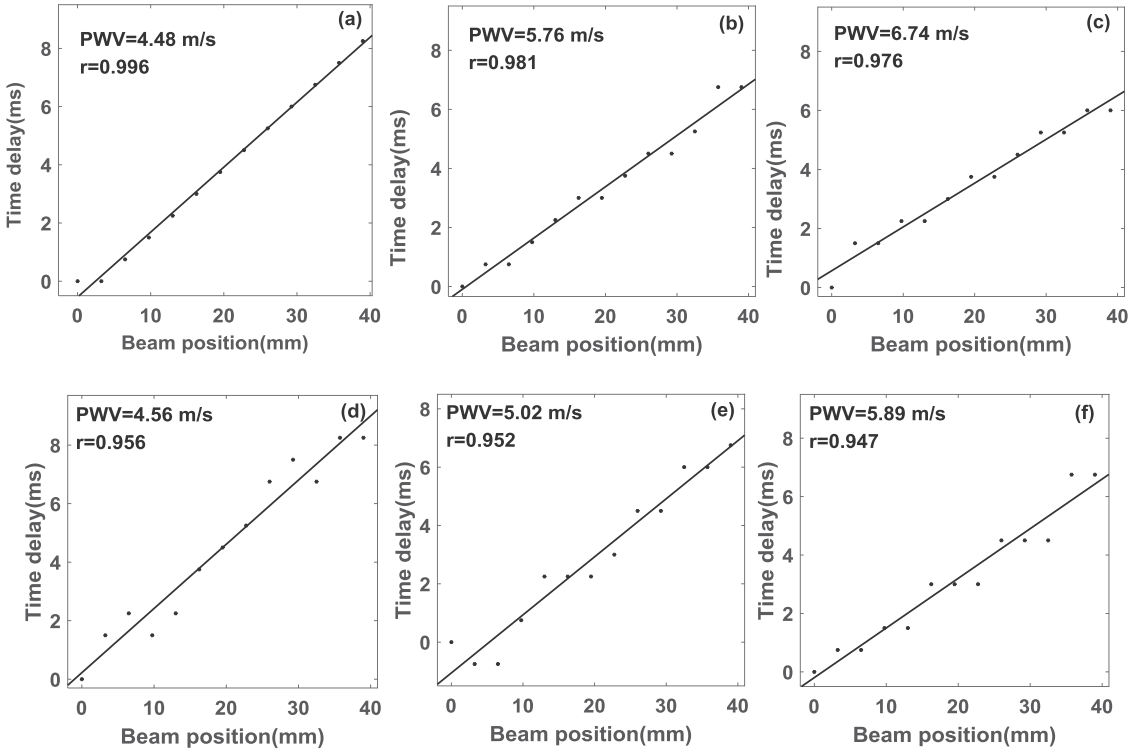

Fig. 11. Beam position dots plotted as function of the TD for the PW propagation as well as the linear regression fitted line for the TH20 (a, b, c) and M2D (d, e, f). The preset PWVs are 4.5 m/s (a, d), 6.0 m/s (b, e), and 7.0 m/s (c, f) for the 24-year-old (a, d), 45-year-old (b, e), and 63-year-old (c, f) subjects, respectively.

estimated IW. The separation performance of the IWs and RWs from the PWs of CCAs has been validated by the correlations between amplitudes of RW and PWV, and cardio-ankle vascular index, respectively [37]. In this method, it is assumed that the upstroke of the blood flow velocity of the axial centerline is caused by the IW. However, the RW might propagate back in the early systolic phase from where there is tapering or stenosis, and thus augment the upstroke blood pressure [43]. In this case, the assumption is invalid, and the accuracy of the extraction of IW and RW could be worsened. This case is not taken into account in this modelling at present. Moreover, the blood vessel is supposed to be elastic to estimate the IW in the Kelvin-Voigt model in spite of the viscoelastic properties of vessel walls. However, it has been demonstrated that the elastic model is acceptable and useful for estimating the IW because the effects of viscous properties of vessel walls are small, particularly for the upstroke period. This enables the simple evaluation of the viscoelastic properties of vessel walls [44].

Attention should be paid that several influence factors encountered in vivo conditions, such as the PW baseline drift induced by respiration or probe movements have been eliminated in the simulation model. Additionally, the parameter settings in present model are based on the conventional focused ultrasound scanning. Through altering simulation setting in Field II, ultrafast ultrasound imaging based on plane wave transmission could be easy generated with the PW propagation model presented in this study. Moreover, the changes in the waveform, amplitude and PWV of the RW are continuous depending on the degree of the arterial stiffness. However, in this study, a limited condition: preset PWVs of 4.5, 6.0, and 7.0 m/s for the clinical data measured from young, middle-aged, and elderly human groups [10], respectively, is set for modelling. An improved model based on a continuous relationship between the PW and arterial stiffness could be useful to perform a precision evaluation study.

5. Conclusions

An ultrasound simulation model incorporating incident and reflected wave propagations along a CCA is proposed to provide a realistic data source for validation of TT-based local PWV estimation algorithms. First, 30 sets of PWs of the vessel walls and blood flow velocities of the axial centerline during a cardiac cycle are estimated on 30 healthy subjects from young, middle-aged, and elderly groups. Then, the corresponding IW and RW are obtained with a velocity- and distension-based upstroke fitting method. The PWs at 13 beam positions along the segment of the CCA of 39 mm are modelled with the preset PWVs of 4.5 m/s, 6.0 m/s, and 7.0 m/s for these three age groups, respectively. With a geometric model of the 39 mm CCA, the dynamic scatterer models for the three age groups are constructed. Finally, the corresponding RF signals are generated in a dynamic scanning mode with a frame rate of 1333 Hz using the Field II platform. To quantitatively evaluate the effectiveness of the proposed simulation model, mean values and SDs for NRMSEs of the three indexes of estimated PW, TD and PWV are calculated. The estimated PWs, TDs, and PWVs are in accordance with the preset ones under different influences of wave reflections. Moreover, the proposed model can characterize the effect of wave reflection on the local PW propagating along CCAs as its clinical manifestation. In conclusion, the proposed ultrasound simulation model can be effective as a realistic data source for the validation of TT-based local PWV estimation algorithms, particularly the effects of RWs on the estimation performance.

Declarations of interest

None.

Conflicts of interest

The work ‘Ultrasound simulation model incorporating incident and reflected wave propagations along a common carotid artery’ is supported by the Grants (81771928 and 61561049) from the National Natural Science Foundation of China, and University Key Lab of Electronic Information Processing of High Altitude Medicine, Yunnan Province. However, such supports do not influence the research work presented here. We certify here that we do not have any financial and personal relationships with other people or organizations that could inappropriately influence our work presented in this manuscript.

Acknowledgements

This work was supported by the Grants (81771928 and 61561049) from the National Natural Science Foundation of China, and University Key Lab of Electronic Information Processing of High Altitude Medicine, Yunnan Province.

Appendix A. Supplementary data

A video containing simulated B-mode scanning images, and a file in .mat format containing the simulated ultrasonic RF echo data for the proposed simulation model are provided, and could be free download at https://doi.org/10.1016/j.compbiomed.2018.11.009 for evaluation.

Supplementary data to this article can be found online at https://doi.org/10.1016/j.compbiomed.2018.11.009.

References

[1] T.W. Hansen, J.A. Staessen, C. Torp-Pedersen, S. Rasmussen, Y. Li, E. Dolan, L. Thijs, J.-G. Wang, E. O'brien, H. Ibsen, Ambulatory arterial stiffness index predicts stroke in a general population, J. Hypertens. 24 (2006) 2247–2253.
[2] I.A. Orlova, E.Y. Nuraliev, E.B. Yarovaya, F.T. Ageev, Prognostic value of changes in arterial stiffness in men with coronary artery disease, Vasc. Health Risk Manag. 6 (2010) 1015.
[3] S. Laurent, P. Boutouyrie, R. Asmar, I. Gautier, B. Laloux, L. Guize, P. Ducimetiere, A. Benetos, Aortic stiffness is an independent predictor of all-cause and cardiovascular mortality in hypertensive patients, Hypertension (Dallas) 37 (2001) 1236–1241.
[4] M. Eren, S. Gorgulu, N. Uslu, S. Celik, B. Dagdeviren, T. Tezel, Relation between aortic stiffness and left ventricular diastolic function in patients with hypertension, diabetes, or both, Heart 90 (2004) 37–43.
[5] G.F. Mitchell, Arterial stiffness and wave reflection in hypertension: pathophysiologic and therapeutic implications, Curr. Hypertens. Rep. 6 (2004) 436–441.
[6] A.P. Guerin, S.J. Marchais, M.E. Safar, G.r.M. London, Impact of aortic stiffness attenuation on survival of patients in end-stage renal failure, Circulation 103 (2001) 987–992.
[7] C.-H. Li, J.-S. Wu, Y.-C. Yang, C.-C. Shih, F.-H. Lu, C.-J. Chang, Increased arterial stiffness in subjects with impaired glucose tolerance and newly diagnosed diabetes but not isolated impaired fasting glucose, J. Clin. Endocrinol. Metabol. 97 (2012) E658–E662.
[8] S. Laurent, J. Cockcroft, L. Van Bortel, P. Boutouyrie, C. Giannattasio, D. Hayoz, B. Pannier, C. Vlachopoulos, I. Wilkinson, H. Struijker-Boudier, Expert consensus document on arterial stiffness: methodological issues and clinical applications, Eur. Heart J. 27 (2006) 2588–2605.
[9] J. Alastruey, Numerical assessment of time-domain methods for the estimation of local arterial pulse wave speed, J. Biomech. 44 (2011) 885–891.
[10] S.I. Rabben, N. Stergiopulos, L.R. Hellevik, O.A. Smiseth, S. Slørdahl, S. Urheim, B. Angelsen, An ultrasound-based method for determining pulse wave velocity in superficial arteries, J. Biomech. 37 (2004) 1615–1622.
[11] P. Segers, A. Swillens, L. Taelman, J. Vierendeels, Wave reflection leads to over-and underestimation of local wave speed by the PU-and QA-loop methods: theoretical basis and solution to the problem, Physiol. Meas. 35 (2014) 847.
[12] A. Eriksson, E. Greiff, T. Loupas, M. Persson, P. Pesque, Arterial pulse wave velocity with tissue Doppler imaging, Ultrasound Med. Biol. 28 (2002) 571–580.
[13] J.M. Meinders, L. Kornet, P.J. Brands, A.P. Hoeks, Assessment of local pulse wave velocity in arteries using 2D distension waveforms, Ultrason. Imag. 23 (2001) 199–215.
[14] R. Williams, A. Needles, E. Cherin, Y.-Q. Zhou, R.M. Henkelman, S.L. Adamson, F.S. Foster, Noninvasive ultrasonic measurement of regional and local pulse-wave velocity in mice, Ultrasound Med. Biol. 33 (2007) 1368–1375.
[15] H.C. Pereira, T. Pereira, V. Almeida, E. Borges, E. Figueiras, J.B. Simoes, J.L. Malaquias, J.M. Cardoso, C.M. Correia, Characterization of a double probe for local pulse wave velocity assessment, Physiol. Meas. 31 (2010) 1449.
[16] Z. Wang, Y. Yang, L.-j. Yuan, J. Liu, Y.-y. Duan, T.-s. Cao, Noninvasive method for measuring local pulse wave velocity by dual pulse wave Doppler: in vitro and in vivo studies, PloS One 10 (2015) e0120482 .
[17] J. Luo, R.X. Li, E.E. Konofagou, Pulse wave imaging of the human carotid artery: an in vivo feasibility study, IEEE Trans. Ultrason. Ferroelectrics Freq. Contr. 59 (2012)

174–181.
[18] F. Li, Q. He, C. Huang, K. Liu, J. Shao, J. Luo, High frame rate and high line density ultrasound imaging for local pulse wave velocity estimation using motion matching: a feasibility study on vessel phantoms, Ultrasonics 67 (2016) 41–54.
[19] H. Hasegawa, K. Hongo, H. Kanai, Measurement of regional pulse wave velocity using very high frame rate ultrasound, J. Med. Ultrason. 40 (2013) 91–98.
[20] J.I. Davies, A.D. Struthers, Pulse wave analysis and pulse wave velocity: a critical review of their strengths and weaknesses, J. Hypertens. 21 (2003) 463–472.
[21] H. Zhang, J.K. Li, A novel wave reflection model of the human arterial system, Cardiovasc. Eng. 9 (2009) 39.
[22] J. Feng, A. Khir, Determination of wave speed and wave separation in the arteries using diameter and velocity, J. Biomech. 43 (2010) 455–462.
[23] E. Hermeling, K.D. Reesink, R.S. Reneman, A.P. Hoeks, Measurement of local pulse wave velocity: effects of signal processing on precision, Ultrasound Med. Biol. 33 (2007) 774–781.
[24] M. Couade, M. Pernot, E. Messas, J. Emmerich, A. Hagege, M. Fink, M. Tanter, Ultrafast imaging of the arterial pulse wave, Irbm 32 (2011) 106–108.
[25] R. Nagaoka, G. Masuno, K. Kobayashi, S. Yoshizawa, S. Umemura, Y. Saijo, Measurement of regional pulse-wave velocity using spatial compound imaging of the common carotid artery in vivo, Ultrasonics 55 (2015) 92–103.
[26] E. Hermeling, K.D. Reesink, L.M. Kornmann, R.S. Reneman, A.P. Hoeks, The dicrotic notch as alternative time-reference point to measure local pulse wave velocity in the carotid artery by means of ultrasonography, J. Hypertens. 27 (2009) 2028–2035.
[27] C. Huang, T.-L. Ren, J. Luo, Effects of parameters on the accuracy and precision of ultrasound-based local pulse wave velocity measurement: a simulation study, IEEE Trans. Ultrason. Ferroelectrics Freq. Contr. 61 (2014) 2001–2018.
[28] R.L. Maurice, M. Bertrand, Speckle-motion artifact under tissue shearing, IEEE Trans. Ultrason. Ferroelectrics Freq. Contr. 46 (1999) 584.
[29] L. Deng, Y. Zhang, X. Hu, L. Gao, Z. Li, The assessment of regional pulse wave velocity accuracy of carotid arteries estimated by using cross-correlation of ultrasound beams, Biomedical Engineering and Informatics (BMEI), 2015 8th International Conference on, IEEE, 2015, pp. 229–233.
[30] J.A. Jensen, Speed-accuracy trade-offs in computing spatial impulse responses for simulating medical ultrasound imaging, J. Comput. Acoust. 9 (2001) 731–744.
[31] X. Zhou, R. Peng, H. Ding, N. Zhang, P. Li, Validation of new and existing decision rules for the estimation of beat-to-beat pulse transit time, BioMed Res. Int. 2015 (2015) 306934.
[32] J. Luo, E.E. Konofagou, A fast normalized cross-correlation calculation method for motion estimation, IEEE Trans. Ultrason. Ferroelectrics Freq. Contr. 57 (2010) 1347–1357.
[33] J. Luo, K. Ying, P. He, J. Bai, Properties of savitzky–golay digital differentiators, Digit. Signal Process. 15 (2005) 122–136.
[34] C. Kasai, K. Namekawa, A. Koyano, R. Omoto, Real-time two-dimensional blood flow imaging using an autocorrelation technique, IEEE Trans. Son. Ultrason. 32 (1985) 458–464.
[35] V.D.W. Jp, M. Siebes, B.E. Westerhof, Comparison of arterial waves derived by classical wave separation and wave intensity analysis in a model of aortic coarctation, Med. Biol. Eng. Comput. 47 (2009) 211–220.
[36] N. Westerhof, P. Segers, B.E. Westerhof, Wave separation, wave intensity, the reservoir-wave concept, and the instantaneous wave-free ratio: presumptions and principles, Hypertension 66 (2015) 93–98.
[37] M. Saito, M. Matsukawa, T. Asada, Y. Watanabe, Noninvasive assessment of arterial stiffness by pulse wave analysis, IEEE Trans. Ultrason. Ferroelectrics Freq. Contr. 59 (2012).
[38] M.S. Olufsen, Structured tree outflow condition for blood flow in larger systemic arteries, Am. J. Physiol. Heart Circ. Physiol. 276 (1999) H257–H268.
[39] A.V. Kamenskiy, Y.A. Dzenis, J.N. Mactaggart, A.S. Desyatova, I.I. Pipinos, In vivo three-dimensional blood velocity profile shapes in the human common, internal, and external carotid arteries, J. Vasc. Surg. 54 (2011) 1011–1020.
[40] J.A. Jensen, A model for the propagation and scattering of ultrasound in tissue, J. Acoust. Soc. Am. 89 (1991) 182–190.
[41] B.H. Mcghee, E.J. Bridges, Monitoring arterial blood pressure: what you may not know, Crit. Care Nurse 22 (2002) 60.
[42] J.D. Parikh, K.G. Hollingsworth, V. Kunadian, A. Blamire, G.A. Macgowan, Measurement of pulse wave velocity in normal ageing: comparison of Vicorder and magnetic resonance phase contrast imaging, BMC Cardiovasc. Disord. 16 (2016) 1–7.
[43] A.D. Hughes, K.H. Parker, J.E. Davies, Waves in arteries: a review of wave intensity analysis in the systemic and coronary circulations, Artery Res. 2 (2008) 51–59.
[44] M. Saito, Y. Yamamoto, M. Matsukawa, Y. Watanabe, M. Furuya, T. Asada, Effect of viscoelasticity of vessel walls on pulse wave, Jpn. J. Appl. Phys. 49 (2010) 07HF12.